Sign inversion in the superconducting order parameter of LiFeAs inferred from Bogoliubov quasiparticle interference

Shun Chi,[1,2] S. Johnston,[1,2,3] G. Levy,[1,2] S. Grothe,[1,2] R. Szedlak,[1] B. Ludbrook,[1,2] Ruixing Liang,[1,2] P. Dosanjh,[1,2] S. A. Burke,[1,2,4] A. Damascelli,[1,2] D. A. Bonn,[1,2] W. N. Hardy,[1,2] and Y. Pennec[1,2]

[1]*Department of Physics and Astronomy, University of British Columbia, Vancouver British Columbia, Canada V6T 1Z1*

[2]*Quantum Matter Institute, University of British Columbia, Vancouver British Columbia, Canada V6T 1Z4*

[3]*Department of Physics and Astronomy, University of Tennessee, Knoxville, Tennessee 37996-1200, USA*

[4]*Department of Chemistry, University of British Columbia, Vancouver British Columbia, Canada V6T 1Z1*

(Received 20 August 2013; revised manuscript received 13 March 2014; published 31 March 2014)

Quasiparticle interference (QPI), by means of scanning tunneling microscopy/spectroscopy (STM/STS), angle-resolved photoemission spectroscopy (ARPES), and multiorbital tight-binding calculations, is used to investigate the band structure and superconducting order parameter of LiFeAs. Using this combination of techniques we identify intraband and interband scattering vectors between the hole (h) and electron (e) bands in the QPI maps. Discrepancies in the band dispersions inferred from previous ARPES and STM/STS are reconciled by recognizing a difference in the k_z sensitivity for the two probes. The observation of both h-h and e-h scattering is exploited using phase-sensitive scattering selection rules for Bogoliubov quasiparticles. From this we demonstrate an $s_\pm$ gap structure, where a sign change occurs in the superconducting order parameter between the e and h bands.

DOI: 10.1103/PhysRevB.89.104522 PACS number(s): 74.55.+v, 74.25.Jb, 74.70.Xa

I. INTRODUCTION

A recurring theme in the study of unconventional superconductors is the pairing of electrons via repulsive interactions [1–4], rather than the attractive interaction mediated by phonons that occurs in conventional superconductors. Cooper pairing driven by a repulsive interaction, such as exchange of antiferromagnetic spin fluctuations, carries a distinguishing feature that the superconducting gap $\Delta(\mathbf{k})$ has changes in sign for different values of momentum $\mathbf{k}$ in the Brillouin zone. This means that identifying the gap symmetry and structure in the high-temperature (high-T_c) iron pnictide superconductors is an essential step towards understanding the origin of superconductivity in these systems [1–4], as well as understanding their relation to the high-T_c cuprates [1].

The electronic structure upon which superconductivity is built in the pnictides consists of hole (h) bands centered at $\mathbf{k} = (0,0)$ and electron (e) bands centered at $\mathbf{k} = (\pm\pi/a, \pm\pi/a)$ [Fig. 1(a)]. In many pnictide systems the h and e bands are strongly nested leading to magnetic instabilities and superconductivity upon doping [3]. This nested multiband structure opens up the possibility that a sign change in momentum space could take the form of an $s_\pm$ gap structure, with $\Delta(\mathbf{k})$ having a different sign on the e and h bands. To date there has been considerable progress in measuring the gap structures in iron pnictide and chalcogenide superconductors [4–18], including many that can discern different gaps associated with the multiple bands crossing Fermi level [6–12], and a few that are sensitive to whether or not there is a sign change between the e and h bands [13–18]. This $s_\pm$ symmetry is believed to be realized in the majority of pnictide superconductors.

LiFeAs has a particularly important place among the pnictides. It is superconducting at its stoichiometric composition, enabling studies of the superconducting state that are undisturbed by the disorder arising from chemical substitutions [19–23]. Furthermore, the system presents a natural cleavage plane between two adjacent Li layers, which leads to stable, nonpolar cleaved surfaces with a carrier density similar to that of the bulk [24]. This makes LiFeAs an ideal system for surface-sensitive probes such as angle-resolved photoemission spectroscopy (ARPES) [7,12,25,26] and scanning tunneling microscopy/spectroscopy (STM/STS) [10,18–20,27,28], and well suited for studying the underlying mechanism of superconductivity in the iron pnictides.

LiFeAs however differs from the other pnictides in some significant ways. The electronic structure of LiFeAs lacks the strong nesting conditions observed in other families, which is the likely reason for the absence of a magnetic phase [25,29]. Moreover, the underlying pairing symmetry in LiFeAs is under debate and it is unclear whether the nature of superconductivity in this material is the same as in the other pnictides.

The lack of nesting between the h and e pockets weakens the traditional argument for $s_\pm$ pairing. This, coupled with the observation of multiple dispersion renormalizations, has led to proposals for an s_{++} pairing symmetry [12] driven by phonon-assisted orbital fluctuations [8,30]. Alternatively, proposals have been made for an exotic triplet pairing. For example, ARPES indicates the presence of a van Hove singularity at the top of the inner hole pockets [25], which can enhance ferromagnetic fluctuations and lead to a p-wave pairing symmetry. This is supported by a recent STM/STS study [18] as well as theory based on the random phase approximation (RPA) and a two-dimensional (2D) three-band model. [31] However, NMR and μSR measurements on high-purity LiFeAs samples do not show any signature of triplet pairing [32–36]. In contrast, there are indications that an $s_\pm$ symmetry is realized in LiFeAs despite the lack of strong nesting between the h and e bands. From a theoretical point of view, both an early functional renormalization group study [based on density functional theory (DFT) band-structure calculations] [37] and a more recent RPA study (based on an ARPES-derived band structure) [38] find a leading $s_\pm$ superconducting instability. This scenario also has experimental support from a number of indirect probes [8,9,33,39].

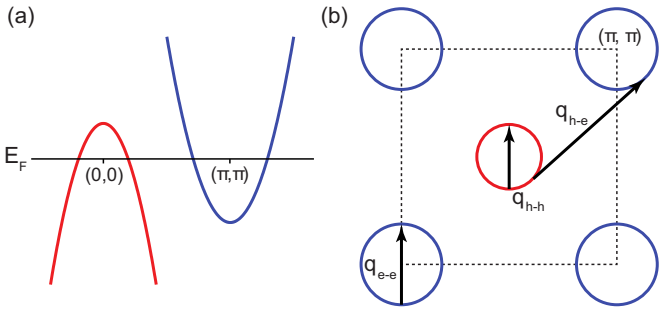

FIG. 1. (Color online) (a) A simplified two-band model for the pnictides with a holelike band centered at $\mathbf{k} = (0,0)$ and an electronlike band centered at $\mathbf{k} = (\pi/a,\pi/a)$. (b) The Fermi surfaces of the bands in (a). The vectors $\mathbf{q}_{h-h}$ and $\mathbf{q}_{e-e}$ show intraband scattering within the hole and electron pockets, respectively, while $\mathbf{q}_{h-e}$ shows interband scattering between the two. In the $s_\pm$ scenario, the sign of $\Delta(\mathbf{k})$ switches sign between the initial and final states of the $\mathbf{q}_{h-e}$ scattering process.

The presence of a spin-resonance mode observed by inelastic neutron scattering is perhaps the strongest indirect evidence in support of the $s_\pm$ gap symmetry in LiFeAs [1,40]. In general, a resonance peak occurs in the imaginary part of the spin susceptibility below T_c at wave vector $\mathbf{Q}$ connecting portions of the Fermi surface that have different signs for the superconducting gap. In LiFeAs, a broad resonance mode is observed at an incommensurate wave vector close to the antiferromagnetic wave vector connecting the h and e bands [8,9,39], consistent with an $s_\pm$ symmetry and similar to other pnictides [13–15]. The observed energy scale Ω_r is consistent with a modulation in LiFeAs's LDOS [19], indicating that this mode may be related to the pairing glue [1]. There are, however, open questions regarding this interpretation. First, the observed spin resonance is rather broad in comparison to the sharp LDOS modulations [19]. Second, in the case of the high-T_c cuprates it was shown that a LDOS modulation in the form of a dip-hump feature is indicative of a pair breaking mode within the Eliashberg formalism [41]. Third, no corresponding feature has been observed in the ARPES spectra as would be expected if the mode was coupling strongly to carriers. In light of these issues we conclude that while the existence of a resonance mode is indicative of a sign change in the order parameter, its role in establishing superconductivity is not fully understood and its presence can only be considered as circumstantial evidence for an $s_\pm$ pairing symmetry.

Given these open issues regarding the pairing symmetry in LiFeAs, it is desirable to have a direct, phase-sensitive measurement of the superconducting gap. Here, we combine ARPES, STM/STS, and multiorbital scattering theory to study quasiparticle interference (QPI) in LiFeAs. Using this coherent approach to determine the electronic structure, we identify the relevant scattering vectors for this system and show that the energy dependence of the QPI intensity behaves as expected for an $s_\pm$ superconductor with scattering from a nonmagnetic potential impurity. In this way we provide direct, phase-sensitive proof for an $s_\pm$ symmetry of the superconducting gap.

The organization of this paper is as follows. In the following section we outline our experimental methods and the details of our model for QPI in LiFeAs. In Sec. III we present results. We begin by summarizing our STM/STS results in Sec. III A. In Sec. III B we identify the scattering vectors in the QPI maps through detailed calculations based on an ARPES-derived band-structure model for LiFeAs. Then, in Sec. III C we examine the intensity variations of the QPI vectors and exploit a set of selection rules to conclude an underlying $s_\pm$ pairing symmetry in this system. We then end in Sec. IV with a summary and some concluding remarks. We give the details of our data treatment for the QPI maps in the Appendix.

II. METHODS

A. Materials and experimental details

Single crystals of LiFeAs ($T_c = 17.2$ K) were grown by a self-flux technique [19,20] first reported by Morozov *et al.* (Ref. [42]). For the STM/STS measurements, a LiFeAs single-crystal sample was cleaved *in situ* at cryogenic temperature below 20 K and inserted into a beetle-type STM head operating under ultrahigh vacuum (UHV) with pressure $P < 1 \times 10^{-9}$ Torr and at a base temperature of 4.2 K. The data was acquired at the STM base temperature 4.2 K, which is the limiting factor for energy resolution. Electrochemically etched tungsten tips were used, which were Ar^+ sputtered, and thermally annealed under UHV prior to measurement. The QPI data were obtained by numerical differentiation of the I-V spectrum acquired at each pixel.

The ARPES measurements were performed with a SPECS Phoibos 150 analyzer and 21.218 eV linearly polarized photons from a monochromatized UVS300 lamp. The LiFeAs single crystals were cleaved *in situ* at a temperature of 6 K in an UHV environment with a base pressure of $P = 5 \times 10^{-11}$ Torr. The full width at half maximum energy and angular resolutions were measured to be 22 meV and 0.025°, respectively. This corresponds to a momentum resolution of 0.001π/a.

B. Multiorbital tight-binding model

To model the electronic dispersion of LiFeAs we modified the ten orbital tight-binding model of Ref. [43], formulated in the two-Fe unit cell. In the normal state, the tight-binding Hamiltonian is given by

$$H_{ns}(\mathbf{k}) = \sum_{\mathbf{k},\sigma} \psi^\dagger_{\mathbf{k},\sigma}\, \hat{h}(\mathbf{k})\, \psi_{\mathbf{k},\sigma}, \qquad (1)$$

where $\psi^\dagger_{\mathbf{k},\sigma} = [c^\dagger_{\mathbf{k},1,\sigma}, \ldots, c^\dagger_{\mathbf{k},10,\sigma}]$ is a row vector of creation operators for the ten Fe orbitals. Here, we follow the notation of Ref. [43] and the matrix representation of the tight-binding Hamiltonian $\hat{h}(\mathbf{k})$ is given therein.

In order to obtain better agreement with the ARPES band structure at $k_z = 0$, a handful of the hopping parameters were adjusted. (A comparison with the ARPES dispersion is shown in Fig. 3, and will be discussed in greater detail below.) Specifically (in the notation of Ref. [43]), we set $\epsilon_1 = -0.235$, $\epsilon_3 = \epsilon_4 = 0.23$, $t^{10}_{18} = 0.211i$, $t^{10}_{27} = -0.258$, $t^{11}_{33} = 0.267$, $t^{11}_{34} = 0.0225$, $t^{10}_{49} = 0.377$, $t^{11}_{001} = 0.0714$, and $t^{101}_{18} = t^{101}_{19} = 0$ (in units of eV). The remaining parameters remain unchanged from those specified in the original model. Finally, the resulting

bands were renormalized by a factor of 2.17, which is typical for the iron pnictides [44].

C. Theory of multiband quasiparticle interference

The QPI patterns are calculated using the usual T-matrix formalism for a single impurity, formulated for a multiorbital system [45]. The single impurity approach is justified by the dilute concentration of impurities observed in our sample [19,20].

First, it is convenient to establish some notation by introducing the band representation for the tight-binding Hamiltonian. We define $\hat{\epsilon}(\mathbf{k}) = \hat{U}(\mathbf{k})\hat{h}(\mathbf{k})\hat{U}(\mathbf{k})^{\dagger}$, where $\hat{\epsilon}(\mathbf{k})$ is understood to be a 10×10 diagonal matrix whose diagonal elements are the eigenvalues of $\hat{h}(\mathbf{k})$ and $U(\mathbf{k})$ is the orthogonal transform diagonalizing $\hat{h}(\mathbf{k})$, which is obtained numerically. We introduce superconductivity in band representation by assigning a momentum-independent instantaneous intraband pairing potential $\Delta_i(\mathbf{k}) = \Delta_i$ to each band. The BCS Hamiltonian is then $H_{bcs} = \sum_{\mathbf{k}} \tilde{\Psi}^{\dagger}_{\mathbf{k}} \tilde{B}(\mathbf{k}) \tilde{\Psi}_{\mathbf{k}}$ where $\tilde{\Psi}^{\dagger}_{\mathbf{k}} = [\tilde{c}^{\dagger}_{\mathbf{k},1,\uparrow}, \ldots, \tilde{c}^{\dagger}_{\mathbf{k},10,\uparrow}, \tilde{c}_{-\mathbf{k},1,\downarrow}, \ldots, \tilde{c}_{-\mathbf{k},10,\downarrow}]$ and

$$\tilde{B}(\mathbf{k}) = \begin{bmatrix} \hat{\epsilon}(\mathbf{k}) & \hat{\Delta} \\ \hat{\Delta} & -\hat{\epsilon}(-\mathbf{k}) \end{bmatrix} \tag{2}$$

is a 20×20 matrix. Here, operators decorated with a tilde $\tilde{A}$ denote operators in band representation and both $\hat{\epsilon}(\mathbf{k})$ and $\hat{\Delta}$ are 10×10 diagonal matrices whose ith diagonal element is the eigenenergy $\epsilon_i(\mathbf{k})$ and pairing potential Δ_i for band i, respectively. Since the impurity must be introduced at the orbital level it is convenient to return to orbital representation by reinserting the orthogonal transformation $\hat{U}(\mathbf{k})$

$$\hat{B}(\mathbf{k}) = \begin{bmatrix} \hat{U}^{\dagger}(\mathbf{k})\hat{\epsilon}(\mathbf{k})\hat{U}(\mathbf{k}) & \hat{U}^{\dagger}(\mathbf{k})\hat{\Delta}\hat{U}^{*}(-\mathbf{k}) \\ \hat{U}^{T}(-\mathbf{k})\hat{\Delta}\hat{U}(\mathbf{k}) & -\hat{U}^{T}(-\mathbf{k})\hat{\epsilon}(-\mathbf{k})\hat{U}^{*}(-\mathbf{k}) \end{bmatrix},$$

where T denotes the transpose, $*$ the complex conjugate, and $\dagger$ the Hermitian conjugate.

In orbital representation, the Green's function for the clean system in the superconducting state is given by

$$\hat{G}_0(\mathbf{k},\omega) = [(\omega + i\delta)\hat{I} - \hat{B}(\mathbf{k})]^{-1}, \tag{3}$$

where δ is a broadening factor and $\hat{I}$ is the 20×20 identity matrix. The impurity-induced Green's function is given by

$$\begin{aligned} \hat{G}(\mathbf{k},\mathbf{p},\omega) &= \hat{G}_0(\mathbf{k},\omega)\delta_{\mathbf{k},\mathbf{p}} + \hat{G}_0(\mathbf{k},\omega)\hat{T}(\mathbf{k},\mathbf{p},\omega)\hat{G}_0(\mathbf{p},\omega) \\ &= \hat{G}_0(\mathbf{k},\omega)\delta_{\mathbf{k},\mathbf{p}} + \delta\hat{G}(\mathbf{k},\mathbf{p},\omega), \end{aligned} \tag{4}$$

where $\hat{T}$ is the T matrix obtained by solving the matrix equation

$$\hat{T}_{\mathbf{kp}}(\omega) = \hat{V}_{\mathbf{kp}} + \frac{1}{N}\sum_{\mathbf{k}'} \hat{V}_{\mathbf{kk}'}\hat{G}_0(\mathbf{k}',\omega)\hat{T}_{\mathbf{k}'\mathbf{p}}(\omega). \tag{5}$$

We consider the LDOS modulations induced by a single impurity that replaces one of the Fe atoms in the two-Fe unit cell. For simplicity we assume that the potential scatterer affects all orbitals on the Fe site in the same way. The impurity Hamiltonian is given by

$$H_{imp} = \sum_{i=1}^{5}\sum_{\mathbf{k},\mathbf{p},\sigma} V_0 c^{\dagger}_{i,\mathbf{k},\sigma} c_{i,\mathbf{p},\sigma}, \tag{6}$$

where the sum over i runs over the five orbitals on one of the Fe sites. Under these assumptions, the T matrix is momentum independent and given by

$$\hat{T}(\omega) = [\hat{I} - \hat{V}\hat{g}(\omega)]^{-1}\hat{V}, \tag{7}$$

where $\hat{g}(\omega) = \frac{1}{N}\sum_{\mathbf{k}} \hat{G}_0(\mathbf{k},\omega)$ and

$$\hat{V} = V_0 \begin{bmatrix} \hat{I} & \hat{0} & \hat{0} & \hat{0} \\ \hat{0} & \hat{0} & \hat{0} & \hat{0} \\ \hat{0} & \hat{0} & -\hat{I} & \hat{0} \\ \hat{0} & \hat{0} & \hat{0} & \hat{0} \end{bmatrix}. \tag{8}$$

Here, each element of the matrix in Eq. (8) represents a 5×5 matrix. The Fourier transform of the impurity induced LDOS modulations $\delta\rho(\mathbf{q},\omega)$ is then given by the trace over the imaginary part of $\delta\hat{G}(\mathbf{k},\mathbf{p},\omega)$

$$\delta\rho(\mathbf{q},\omega) = \frac{i}{N}\sum_{\mathbf{k}}\sum_{i=1}^{10}[\delta\hat{G}_{ii}(\mathbf{k},\mathbf{k}+\mathbf{q},\omega) - \delta\hat{G}^{*}_{ii}(\mathbf{k}+\mathbf{q},\mathbf{k},\omega)]. \tag{9}$$

For our calculations we took $V_0 = 50$ meV, however our conclusions are not sensitive to this value. Furthermore, we assumed superconducting gap values of $\Delta_{h_1} = \Delta_{h_2} = 7$ meV, $\Delta_{h_3} = 3$ meV, and $\Delta_{e_{1,2}} = -4$ meV [7,12]. Note that since we restrict our simulations to energies above the gap edges, the precise choice in Δ_i values is not critical to our identification of the QPI wave vectors.

D. Phase sensitivity

STM/STS provides access to the phase of the superconducting gap by imaging QPI of Bogoliubov quasiparticles, which are a superposition of e and h excitations. The QPI patterns are imaged in real space by measuring the differential conductance dI/dV between the tip and sample as a function of position $\mathbf{r}$ and energy E [Fig. 2(a)]. A Fourier transform of this image produces a $\mathbf{q}$-space QPI intensity map [Fig. 2(c)], where peaks occur at wave vectors connecting segments of the band structure [Fig. 1(b)] [5].

The phase sensitivity arises from the coherence factors $u_i(\mathbf{k})$ and $v_i(\mathbf{k})$, which determine the degree of e and h admixture (i is a band index). This is most easily understood by examining the scattering rate between initial and final states as determined by Fermi's golden rule. In the multiband superconductor the scattering rate for transitions between band i and f is proportional to [46]

$$\begin{aligned} W_{i\to f}(\mathbf{k},\mathbf{k}') \propto\ & |u_i(\mathbf{k})u^{*}_f(\mathbf{k}') \pm v_i(\mathbf{k})v^{*}_f(\mathbf{k}')|^2 \\ & \times |V(\mathbf{k}'-\mathbf{k})|^2 N_i(\mathbf{k})N_f(\mathbf{k}'), \end{aligned} \tag{10}$$

where $V(\mathbf{q})$ is the scattering potential at vector $\mathbf{q} = \mathbf{k}' - \mathbf{k}$ and $N_i(\mathbf{k})$ the partial density of states of band i. The negative and positive signs in Eq. (10) correspond to scattering from a potential and a magnetic impurity, respectively. The phase of $\Delta_i(\mathbf{k})$ enters via the Bogoliubov coherence factors

$$\begin{aligned} v_i(\mathbf{k}) &= \mathrm{sign}[\Delta_i(\mathbf{k})]\sqrt{\frac{1}{2}\left(1 - \frac{\epsilon_i(\mathbf{k})}{E_i(\mathbf{k})}\right)}; \\ u_i(\mathbf{k}) &= \sqrt{1 - |v_i(\mathbf{k})|^2}. \end{aligned} \tag{11}$$

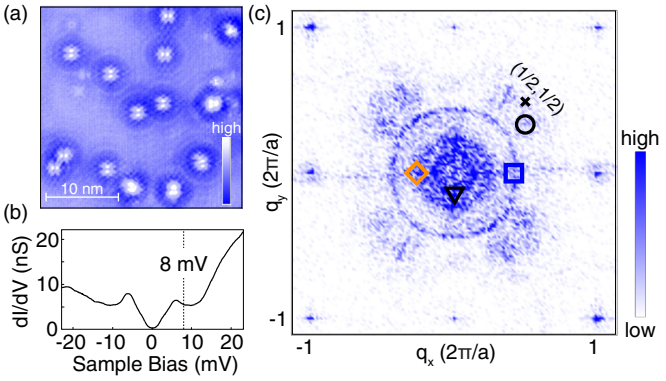

FIG. 2. (Color online) (a) A 26×26 nm^2 dI/dV tunneling conductance map at $V_s = 8$ mV, which is outside the superconducting gaps. Fourteen distinct defects are observed, ten of which are Fe-D_2 defects. (b) A typical dI/dV spectrum out of the original 400×400 pixel grid, selected from a pristine area. The rise in dI/dV at $V_s > 12$ mV is a reproducible feature across every sample measured. (c) The QPI map obtained from a filtered Fourier transform of the conductance map. (Filtering procedures are detailed in Appendix.) Scattering among the hole bands appears as rings centered at $\mathbf{q} = (0,0)$ while interband scattering between the hole and electron bands appears as arcs centered around $\mathbf{q} = (\pm\pi/a, \pm\pi/a)$. The symbols in (c) indicate the location of the QPI vectors whose dispersion is tracked in Fig. 3.

The term $|u_i(\mathbf{k})u_f^*(\mathbf{k}') \pm v_i(\mathbf{k})v_f^*(\mathbf{k}')|$ is close to 1 for energies well outside the superconducting gaps, independent of the pairing phase. Close to or below the superconducting gap, where Bogoliubov quasiparticles play an important role, $v_i(\mathbf{k})$ and $u_i(\mathbf{k})$ become comparable in magnitude. Thus the term $|u_i(\mathbf{k})u_f^*(\mathbf{k}') \pm v_i(\mathbf{k})v_f^*(\mathbf{k}')|$ becomes a momentum-dependent prefactor differing from 1 depending on the relative sign of $\Delta(\mathbf{k})$ and $\Delta(\mathbf{k}')$. This establishes a set of selection rules that will enhance or suppress the scattering rate near the superconducting edge relative to the rate measured above it. Thus the QPI intensity is sensitive to the nature of the impurity and the relative sign of $\Delta_i(\mathbf{k})$ and $\Delta_f(\mathbf{k}')$. These selection rules can also be more rigorously derived using the T-matrix formalism [47,48].

The selection rules for the pnictide band structure shown in Fig. 1 are summarized in Table I for the cases of an s_{++} and $s_{\pm}$ pairing symmetry. For instance, in the $s_{\pm}$ scenario with nonmagnetic impurities one expects the intensity of QPI vectors associated with interband scattering between the hole and electron bands $\mathbf{q}_{h-e}$ to be enhanced while intraband scattering within the hole bands or the electron bands $\mathbf{q}_{h-h}$ and $\mathbf{q}_{e-e}$, respectively, is suppressed when sweeping the bias voltage from above to inside the superconducting gap. Finally, we emphasize here that both the symmetry and nature of the impurity can be uniquely inferred from relative behavior of subsets of the QPI intensities as indicated in Table I.

TABLE I. A summary of the QPI selection rules expected for a pnictide superconductor with s_{++}, $s_{\pm}$. The QPI intensity of a scattering vector is either suppressed or enhanced inside the superconducting gap relative to the intensity outside the gap. The intensity variations stem from the energy dependence of the prefactor in Eq. (10). The four combinations of two pairing symmetries and two kinds of impurities result in four distinct sets of selection rules that can uniquely identify the pairing symmetry and the nature of the impurity.

Scenario	$\mathbf{q}$ Suppressed Intensity	$\mathbf{q}$ Enhanced Intensity
nonmag. imp., s_{++}	$\mathbf{q}_{h-h}$, $\mathbf{q}_{e-e}$, $\mathbf{q}_{h-e}$	-
mag. imp., s_{++}	-	$\mathbf{q}_{h-h}$, $\mathbf{q}_{e-e}$, $\mathbf{q}_{h-e}$
nonmag. imp., $s_{\pm}$	$\mathbf{q}_{h-h}$, $\mathbf{q}_{e-e}$	$\mathbf{q}_{h-e}$
mag. imp., $s_{\pm}$	$\mathbf{q}_{h-e}$	$\mathbf{q}_{h-h}$, $\mathbf{q}_{e-e}$

III. RESULTS

A. QPI maps

A summary of our STM/STS measurements ($T = 4.2$ K) is given in Fig. 2. Figure 2(a) shows a 26×26 nm^2 tunneling conductance map of our sample taken at $V_s = 8$ mV. Figure 2(b) shows a typical dI/dV spectrum at a location far from any defect. A clear $\Delta = 6$ meV superconducting gap is resolved along with a subtle shoulder at $\sim$3 meV. These values are consistent with the full double gap structure found in the same sample at lower temperature ($T = 2$ K) [19,20]. A rapidly decaying diffraction pattern is present around each defect [Fig. 2(a), resulting from modulations of the local density of states (LDOS) due to quasiparticle scattering. The corresponding QPI map [the two-dimensional power spectrum of Fig. 2(a)] is shown in Fig. 2(c). Here we have applied a real-space and momentum-space Gaussian mask method to remove a signal arising from the defect centers that obscures the QPI intensity. The details of this procedure are given in the Appendix. No symmetrization has been applied to the data. Therefore, the symmetry of our QPI intensity map is certain to reflect the original symmetry of the underlying electronic structure.

The Bragg diffraction peaks of the As/Li $[(2\pi/a,0)]$ and Fe $[(2\pi/a,2\pi/a)]$ sublattices are clearly resolved at the outer edge of the QPI map. In addition to the Bragg peaks, we find three features centered on $\mathbf{q} = (0,0)$: two small inner rings and a larger outer ring, in agreement with previous studies [10,18]. We also observe a set of arc features located midway along the $(0,0) - (\pm 2\pi/a, \pm 2\pi/a)$ directions. Similar features were observed in Ref. [9], but these features were at the edge of the data presented. These rings and arcs originate from multiple interband and intraband scattering processes, and due to the complexity of the multiband electronic structure, their specific assignment has been controversial [10,28]. Allan *et al.*, (Ref. [10]) assigned the three rings to intraband scattering within the three h bands. However, the size of the bands inferred from this interpretation is inconsistent with ARPES measurements. This was pointed out by Hess *et al.* (Ref. [28]), who interpreted the inner and outer rings as intraband scattering within two h bands, and the middle ring as interband scattering between the two. No assignment for the arclike features has been made to date.

B. Identification of the scattering vectors

To identify the underlying bands associated with each of these vectors, QPI maps were modeled using the T-matrix

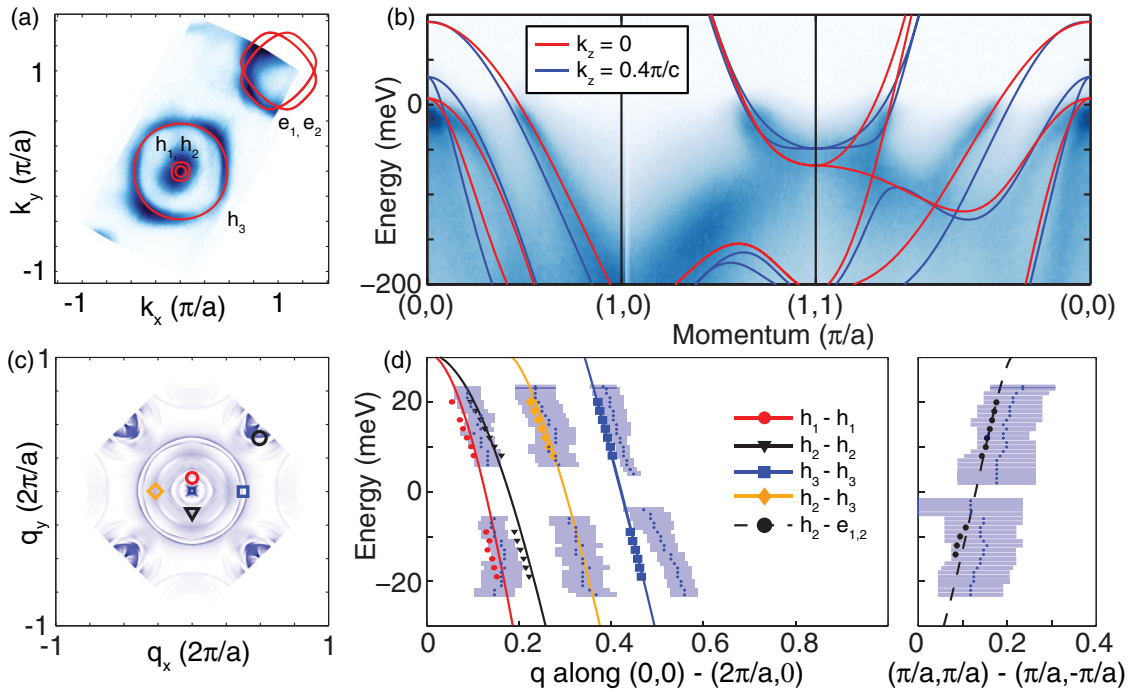

FIG. 3. (Color online) (a) The Fermi surfaces obtained from ARPES (shaded) and the model (solid lines). (b) The ARPES and model dispersions along the high-symmetry cuts of the first Brillouin zone. In (a) and (b) the ARPES spectra are shown for a photon energy that selects k_z values near zero. The model dispersions are shown for $k_z = 0$ (red) and $k_z = 0.4\pi/c$ (blue). (c) The calculated QPI at $V = 8$ mV assuming that electrons tunnel into a nonzero $k_z = 0.4\pi/c$. Features associated with intraband and interband transitions are indicated by the open symbols. (d) The experimental (blue points with error bars) and theoretical (solid symbols) dispersion of the QPI vectors indicated in (c). The error bars are determined approximately by the full width at half maximum of the QPI features plus one additional pixel uncertainty. The solid lines show the dispersion expected from the model dispersion.

formalism outlined in Sec. II C. In order to accurately identify each of the vectors observed it is important to anchor the model electronic structure to the empirical band structure observed by ARPES, as shown in Figs. 3(a) and 3(b). With a photon energy of 21.2 eV, and based on an inner potential $V_0 = 15.4$ eV [49], ARPES maps the electronic excitations for $\mathbf{k}_{||}$ spanning the first Brillouin zone at the average perpendicular momentum $k_z = 2.93 \times 2\pi/c$, where $c = 6.31$ Å is the lattice parameter perpendicular to the (100) surface [23]. This selects a $\mathbf{k}_{||}$ plane intersecting the three-dimensional dispersion close to the Γ point [up to a reciprocal lattice vector $\mathbf{G} = (0,0,6\pi/c)$, or $k_z \sim 0$ in a higher Brillouin zone] [50]. The Fermi surface along this $\mathbf{k}_{||}$ plane [Fig. 3(a)] is composed of two hole pockets centered at Γ (denoted h_2 and h_3) and two electron pockets centered at each of the M points (denoted e_1 and e_2). A momentum distribution curve analysis of the ARPES spectra indicates the presence of a third inner hole pocket h_1, with the tops of the h_1 and h_2 bands located within a ±6 meV window of E_F. To model this electronic structure, we adopted the modified two-Fe ten-orbital tight-binding model introduced in Sec. II B. The band dispersion for this model is shown in Figs. 3(a) and 3(b).

The calculated QPI intensity map at $V = 8$ mV, based on this model of the band structure, is shown in Fig. 3(c), where we have assumed that electrons tunnel into a nonzero $k_z = 0.4\pi/c$ cut of the three-dimensional band structure [43,49]. (We will return to this point shortly.) A number of QPI vectors are present in the calculation, and are highlighted by the open symbols. The calculation identifies the two innermost rings (red ◯ and black ▽) and the outermost large ring (blue □) with intraband scattering between three hole bands, h_1-h_1, h_2-h_2, and h_3-h_3, respectively. The third ring from the center (orange ◇) is due to interband scattering between the inner and outer hole bands h_1-h_3 and h_2-h_3. Our model also identifies the arclike features (black ◯) centered on $(\pm\pi/a, \pm\pi/a)$ with scattering between the h_2 and $e_{1,2}$ bands. Scattering between the h_3 and $e_{1,2}$ bands is suppressed due to a mismatch of orbital character in these two bands.

Comparing to the experiment we associate the smallest to largest of the three QPI rings in Fig. 2(c) with h_2-h_2, h_2-h_3, and h_3-h_3 scattering, respectively, and the arcs with h_2-$e_{1,2}$ scattering. It should be noted that the consistency between the simulation with only an intraorbital scattering potential [see Fig. 3(c)] and the experimental QPI image [see Fig. 2(c)] implies that quasiparticle scattering primarily occurs between states with the same orbital character. These assignments are qualitatively consistent with Ref. [28], however, the dispersion of the QPI vectors quantitatively disagrees with the ARPES band dispersion near the Γ point (again, measured here a point related to Γ by a reciprocal lattice vector). Notably, our ARPES measurements indicate that the top of h_2 is no more than 6 meV above E_F at Γ; above this energy the h_2-h_2 and h_2-h_3 features should vanish due to phase space constraints if STM is probing the band structure in the $k_z = 0$ plane. This is inconsistent with the observed QPI dispersions, shown in Fig. 3(d) (data points with error bars) where all of the rings disperse to energies >20 meV. In ARPES experiments the

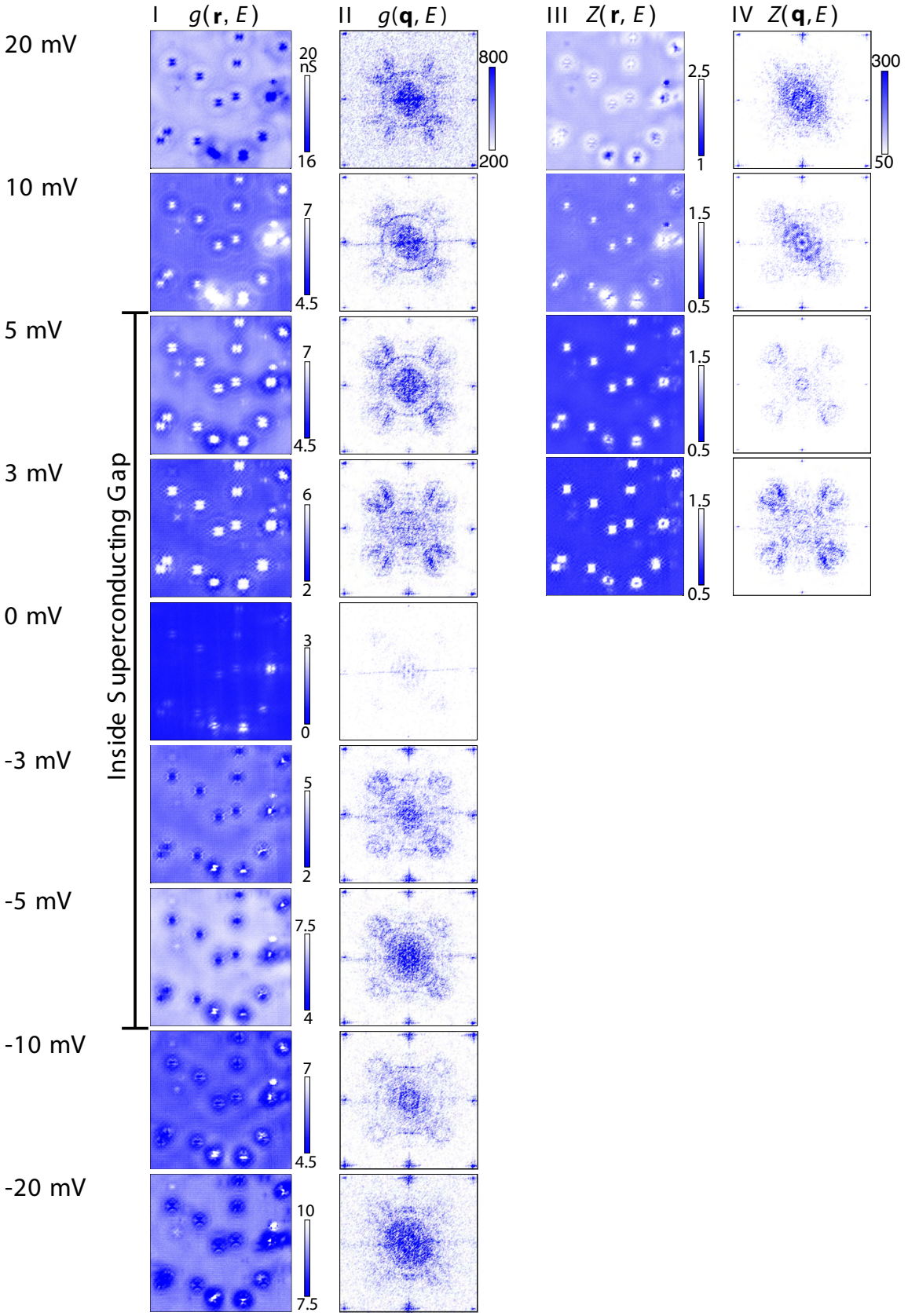

FIG. 4. (Color online) The energy dependence of the conductance maps $g(\mathbf{r},eV)$ (column I) and their corresponding Fourier transforms $g(\mathbf{q},eV)$ (column II). In computing $g(\mathbf{q},eV)$ at each energy we use the same parameters for Gaussian mask and Gaussian suppression (see Appendix). In addition, QPI images in the second column are all plotted on the same color scale so that the relative intensities can be directly compared. The corresponding real space Z maps defined as $Z(\mathbf{r},eV) = g(\mathbf{r},eV)/g(\mathbf{r}, -eV)$ are shown in column III, while the Fourier transform $Z(\mathbf{q},eV)$ are shown in column IV in the same color scale.

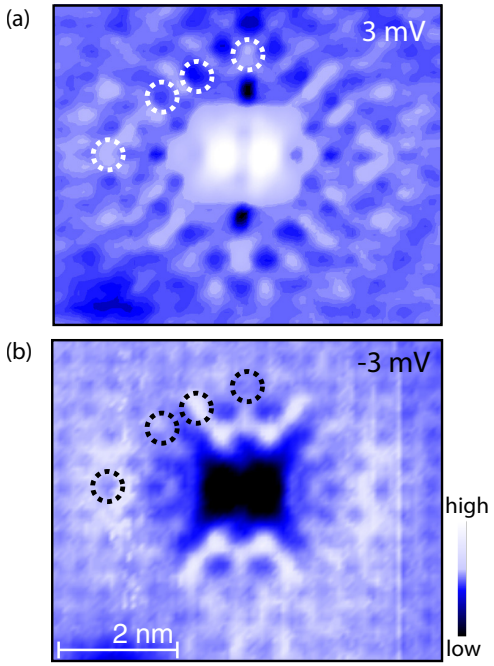

FIG. 5. (Color online) Tunneling conductance maps dI/dV in the vicinity of an Fe-D_2 defect at (a) $V_s = +3$ mV and (b) $V_s = -3$ mV. The antiphase relationship of the local density of states modulations is highlighted by the locations with high intensities inside the white circles of (a) and the corresponding low intensities inside black circles of (b), and vice versa.

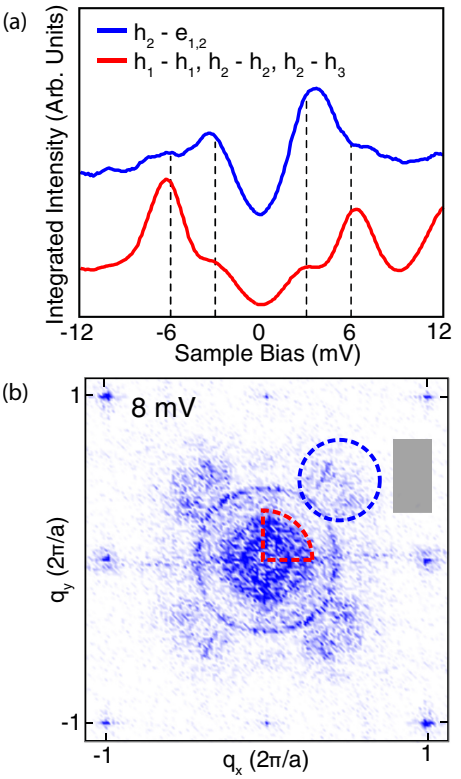

FIG. 6. (Color online) (a) The integrated intensity of the QPI signal for the intraband h-h (red) and interband h-e (blue) scattering vectors. The curves were then normalized to the value at 12 meV and the interband intensity has been offset for clarity. The dashed lines indicate the values of the superconducting gaps. (b) The red sector and blue circle are the integration windows for intraband h-h and interband h-e scattering intensities in (a), respectively. A noise background signal is integrated in the gray rectangular area and subtracted. Here the windows are shown in one quarter for simplicity but the integration is performed over the equivalent areas in all four quadrants of the image.

value of k_z can be controlled via varying the incident photon energy and our photon energy corresponds to $k_z \sim 0$. However, in the case of STS/STM, it is less clear which values of k_z are probed in a bulk 3D system. Empirically we have found that $k_z = 0.4\pi/c$ provides good agreement between our model and the data [Fig. 3(d)]. The solid symbols plot the dispersion of the calculated QPI features. The agreement between the model and the experiment is good and a nonzero value of k_z reconciles differences in band structure inferred from ARPES and STM/STS measurements [10,12,28]. We note that the agreement may be further improved by integrating signal over a range of k_z values. However, this would required an explicit calculation of the tunneling matrix element and is left for future work.

The fact that the inner hole pocket(s) disperse well above 20 meV at finite k_z implies that a weak nesting condition exists between small inner hole pockets and comparatively large electron pockets at the Fermi level. This is consistent with a weak and incommensurate spin-resonance mode revealed by inelastic neutron scattering (INS) at a wave vector linking the h and e pockets [8,9]. Furthermore, we observe a distinct scattering process between the hole and electron Fermi surface sheets h_2-$e_{1,2}$, which, unlike the similar feature in Fe(Se,Te) [17], is well separated from the commensurate (π,π) point. This allows us to unambiguously disentangle QPI of h-e scattering from Bragg peaks of possible charge or magnetic ordering [51].

C. Variation of the QPI intensity and $s_\pm$ pairing

Now that the QPI vectors have been identified, we turn to identifying the symmetry of the order parameter. This is accomplished by an examination of QPI of Bogoliubov quasiparticles near the superconducting gap, where the selection rules discussed in Sec. II become dominant. They are reflected in the intensity variations in the QPI maps. The energy dependence of the conductance maps and QPI intensities are shown in Fig. 4. The first and second columns of Fig. 4 show the real and momentum space QPI maps. For completeness, the third column shows the so-called Z maps in real space, defined as the ratio of the conductance maps at positive and negative biases $Z(\mathbf{r},E) = g(\mathbf{r},E)/g(\mathbf{r},-E)$ [52]. The fourth column is the corresponding Fourier transform $Z(\mathbf{q},E)$.

For biases well above the superconducting gap, the intensities of different scattering vectors in the QPI maps are relatively energy independent; for example, compare the QPI maps at $V = 10$ and 20 mV. In contrast, as the bias voltage sweeps from above the gap [Fig. 4 $g(\mathbf{q},eV)$ at 10 meV] to inside the gap [Fig. 4 $g(\mathbf{q},eV)$ at 3 mV], the intensity of the intraband and interband h scattering is strongly suppressed while the interband h-e scattering is significantly enhanced.

QPI of Bogoliubov quasiparticles distinguishes itself from normal state QPI by an antiphase relation of LDOS modulations at positive and negative energies [52,53]. We illustrate

this in Figs. 5(a) and 5(b), which show LDOS modulations near an Fe-D_2 defect at ± 3 mV [20]. The antiphase relation is apparent in the contrast inversion highlighted inside the dashed circles in Fig. 5. This confirms the dominance of Bogoliubov QPI inside the superconducting gap. Z maps emphasize the antiphase component of Bogoliubov QPI while suppressing the in-phase component of normal state QPI [52,53]. $Z(\mathbf{r},eV)$ at 3 mV (see Fig. 4) shows strong short-wavelength real-space modulations (column III) near each impurity. The Fourier transform $Z(\mathbf{q},E = 3\ \text{meV})$ reveals strong intensity arcs near $(\pm\pi/a, \pm\pi/a)$, corresponding to the previously identified e-h scattering vectors. The intensity of these arcs diminishes as the bias voltage sweeps from inside the large gap to above it. Therefore the intensity variations observed in this energy range are indeed due to the selection rules imposed by the symmetry of the order parameter.

We further quantify these intensity variations shown in Fig. 4 by examining the integrated weight of each QPI vector as a function of energy, as shown in Fig. 6(a). Here, the intraband h-h and interband h-e scattering vectors are isolated by defining appropriate integration windows shown in Fig. 6(b). The integrated intensity follows the behavior reflected in the dI/dV maps, demonstrating the selection rules for the entire data set.

Comparing to the selection rules in Table I, we find that the data is most consistent with an $s_\pm$ scenario with $\Delta(\mathbf{k})$ changing sign between the h and e bands; below the superconducting gap h-h scattering intensities are suppressed while e-h scattering intensities are enhanced for nonmagnetic impurities [45,47]. Magnetic impurities in the $s_\pm$ scenario have the opposite effect. The observed selection rules are also distinct from the s_{++} scenario with either magnetic or nonmagnetic impurities, see Table I. Furthermore, by considering that Knight shift decreases below T_c [32,34,35], we rule out the chiral p-wave state. Our results indicate the nonmagnetic nature of the most common defect. This is consistent with the expectation that the Fe-D_2 defect is most likely a Li substitution on an Fe site, or an Fe vacancy [20], both of which are expected to be nonmagnetic. We therefore infer that the only candidate consistent with our measurements is an $s_\pm$ symmetry.

IV. SUMMARY AND CONCLUSIONS

We have examined QPI in LiFeAs using a combination of STM/STS, ARPES, and a tight-binding model. By anchoring our tight-binding description of LiFeAs to the ARPES-derived band dispersions we were able to unambiguously assign each of the scattering vectors in the QPI maps. In this framework, we have reconciled not only the discrepancies in the assignments of scattering vectors in prior QPI studies but also the disagreement on the sizes of inner hole pockets between ARPES and STM techniques by recognizing a nontrivial k_z dependence in the tunneling process. With the assignment of the scattering vectors made, we then examined the detailed variations of the QPI intensity as a function of bias voltage. The variations in intensity near the superconducting gap are only consistent with an $s_\pm$ pairing symmetry where the change in sign occurs between the electron and hole pockets. Together with the observation of a spin fluctuation resonance by INS [8,9], this work presents a compelling evidence of unconventional $s_\pm$ pairing in LiFeAs driven by repulsive spin fluctuation interactions. This implies LiFeAs shares a common superconducting mechanism with the other members in the iron pnictide family [1–4]. Hence LiFeAs is a simple and clean model material for probing the common physics of iron pnictides.

This work also demonstrates how Bogoliubov QPI from defect/impurity scattering provides a direct phase-sensitive measurement of superconducting pairing symmetry. Bogoliubov QPI has been used to confirm the sign flip in the d-wave $Ca_{2-x}Na_xCuO_2Cl_2$ cuprate superconductor [54] as well as Fe(Se,Te) iron-based superconductor [17] under high magnetic field, where vortices behaved as magnetic scattering centers. However, this method is only suitable for materials with very short superconducting coherence lengths so that a vortex can be treated as a localized strong magnetic scattering center. Here Bogoliubov QPI is measured (without the application of a magnetic field) by taking advantage of point defects/impurities inside the material, which has been proposed only theoretically [45,47,48]. This method can be generalized to other superconductors, provided the nature (magnetic vs nonmagnetic) of the impurities are known.

ACKNOWLEDGMENTS

S.C. and S.J. contributed equally to this work. The authors acknowledge I. Elfimov, C. Hess, P. J. Hirschfeld, A. Kemper, I. I. Mazin, G. A. Sawatzky, E. van Heumen, and P. Wahl for discussions. This work was supported by the Killam Foundation, Alfred P. Sloan Foundation, NSERC's Steacie Memorial Fellowship (A.D.), the Canada Research Chairs Program (A.D., S.B.), CFI, NSERC, and CIFAR Quantum Materials. This work was made possible in part by the facilities of the Shared Hierarchical Academic Research Computing Network and Compute/Calcul Canada.

APPENDIX: DATA PROCESSING METHODS

In this Appendix we outline our data processing method for the QPI maps shown in the main text. Figures 7(a) and 7(b) show the tunneling conductance maps $g(\mathbf{r},V)$ at $V = 8$ mV and its direct Fourier transform $g(\mathbf{q},V)$, respectively. Although there are obvious Friedel oscillations around each defect, the Fourier-transformed image does not show a clear QPI pattern due to a dominant background signal centered at $q = (0, 0)$. Here, we employ two methods to remove this background and recover the underlying QPI patterns.

As shown in Fig. 7(a), $g(\mathbf{r},8\ \text{mV})$ exhibits strong conductance peaks at the defect centers that give rise to a strong background signal in momentum space, overwhelming the QPI signal. In general, the tunneling conductance map $g(\mathbf{r},E = eV) = dI/dV(\mathbf{r},eV)$ is given by

$$g(\mathbf{r},\ eV) = \frac{eI_tN(\mathbf{r},\ eV)}{\int_0^{eV_s} N(\mathbf{r},\ E)\,dE}, \tag{A1}$$

where e is a unit charge, $N(\mathbf{r},eV)$ is the LDOS at $\mathbf{r}$, and $E =$ eV, and V_s is the setting bias voltage for I-V spectra [52]. According to Eq. (A1) the variation of $g(\mathbf{r},E = \text{eV})$ is directly proportional to the variation of the LDOS if the normalization $\int_0^{eVs} N(\mathbf{r},eV)dE$ is spatially homogeneous. This

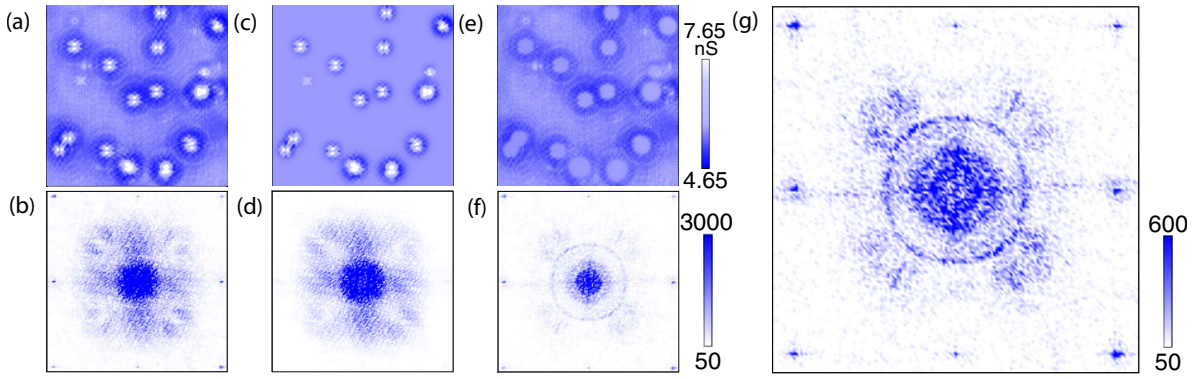

FIG. 7. (Color online) Examples of the processing techniques for the STM/STS data. (a) The tunneling conductance map $g(\mathbf{r},8\text{ meV})$ and (b) its Fourier transform. (c) The portion of the 8 mV conductance map removed from the defect centers and (d) its corresponding Fourier transform. (e) Masked tunneling conductance map $g_M(\mathbf{r},8\text{ meV})$ and (f) its corresponding Fourier transform. (d) The resulting QPI pattern. (a), (c), and (e) are in the same color scale as indicated next to (e); (b), (d), and (f) are in the same color scale as indicated next to (f). The major contribution to the raw signal in (a) comes from the defect centers (b). (g) shows the final QPI map after the additional application of the Gaussian suppression method of Ref. [10].

condition however, does not hold at the center of the defects when the defects strongly modify the local potential. This is because $N(\mathbf{r},E)$ can be dramatically modified by local changes in the electronic structure and/or the creation of bound states. The LDOS of LiFeAs is highly inhomogeneous near E_F [19], so the defect-induced changes in the local electronic structure cause a significant variation in the integral of the LDOS over the energy range [0,25 meV]. In addition, all common defects in LiFeAs generate bound states inside the superconducting gaps [20]. Therefore, the behavior of $g(\mathbf{r},E)$ at defect centers cannot be simply interpreted as Friedel oscillations in $N(\mathbf{r},E)$ due to the inhomogeneity of the normalization factor.

A Gaussian masking method is used to eliminate the signal from the central conductance peaks of these defects. For a defect located at $\mathbf{r}_0$, the masked conductance map $g_M(\mathbf{r},E)$ is given by $g_M(\mathbf{r},E) = g(\mathbf{r},E) \times [1 - M(\mathbf{r}-\mathbf{r}_0,\sigma)]$, where $M(\mathbf{r}-\mathbf{r}_0,\sigma)$ is a truncated Gaussian function with the maximum value $= 0.99$ and σ is the standard deviation, taken to be approximately the half width of the defect center. This Gaussian masking method suppresses the local conductance peaks associated with the defect centers yet preserves the sign of $g(\mathbf{r},E)$ and produces a smooth transition from the masked regions to the QPI nearby. We apply the Gaussian mask to each of the defects. Figures 7(c) and 7(d) show the portion of the real space conductance map removed by the mask and its corresponding Fourier transform, respectively. This demonstrates that the defect centers primarily contribute a large background signal centered at $\mathbf{q} = (0, 0)$. Figures 7(e) and 7(f) show the real-space and momentum-space conductance maps after the application of the Gaussian mask, respectively. After the removal of the defect center's background signal, significantly more symmetric and regular patterns stand out in momentum space. A small but high-intensity ring is present in the center and is surrounded by a second less intense ring and a third larger ring. In addition, arc structures appear in the direction (0,0)-$(\pm 2\pi/a, \pm 2\pi/a)$. In the analysis, no symmetrization has been applied to the data. Thus any feature satisfying the tetragonal crystal symmetry is real and originates from the underlying electronic structure.

As shown in Fig. 7(f), the strong intensity around $\mathbf{q} = (0,0)$ lowers the visibility of the QPI pattern at larger $\mathbf{q}$. We therefore further applied the Gaussian suppression method of Allan *et. al.* [10] to suppress the central peak: $g(\mathbf{q},E) = g_{raw}(\mathbf{q},E) \times [1 - 0.95 \times G(\mathbf{q},\sigma)]$, where $G(\mathbf{q},\sigma)$ is a Gaussian function with peak value $= 1$ and $\sigma \sim 0.35\pi/a$. We chose to retain 5% of the signal at $\mathbf{q} = (0,0)$ in order to not overly suppress the real QPI signal near $\mathbf{q} = (0,0)$. Figure 7(g) shows the final QPI map after applying both the Gaussian mask in real space and Gaussian suppression in momentum space. We emphasize that the same treatment with the same masking parameters was applied to all of the QPI maps.

[1] D. J. Scalapino, Rev. Mod. Phys. **84**, 1383 (2012).
[2] J. Kondo, Prog. Theor. Phys. **29**, 1 (1963).
[3] I. I. Mazin, D. J. Singh, M. D. Johannes, and M. H. Du, Phys. Rev. Lett. **101**, 057003 (2008).
[4] P. J. Hirschfeld, M. M. Korshunov, and I. I. Mazin, Rep. Prog. Phys. **74**, 124508 (2011).
[5] C. L. Song and J. E. Hoffman, Curr. Opin. Solid State Mater. Sci. **17**, 39 (2013).
[6] H. Ding, P. Richard, K. Nakayama, K. Sugawara, T. Arakane, Y. Sekiba, A. Takayama, S. Souma, T. Sato, T. Takahashi, Z. Wang, X. Dai, Z. Fang, G. F. Chen, J. L. Luo, and N. L. Wang, Europhys. Lett. **83**, 47001 (2008).
[7] K. Umezawa, Y. Li, H. Miao, K. Nakayama, Z.-H. Liu, P. Richard, T. Sato, J. B. He, D.-M. Wang, G. F. Chen, H. Ding, T. Takahashi, and S.-C. Wang, Phys. Rev. Lett. **108**, 037002 (2012).
[8] A. E. Taylor, M. J. Pitcher, R. A. Ewings, T. G. Perring, S. J. Clarke, and A. T. Boothroyd, Phys. Rev. B **83**, 220514(R) (2011).
[9] N. Qureshi, P. Steffens, Y. Drees, A. C. Komarek, D. Lamago, Y. Sidis, L. Harnagea, H.-J. Grafe, S. Wurmehl, B. Büchner, and M. Braden, Phys. Rev. Lett. **108**, 117001 (2012).
[10] M. P. Allan, A. W. Rost, A. P. Mackenzie, Yang Xie, J. C. Davis, K. Kihou, C. H. Lee, A. Iyo,

H. Eisaki, and T.-M. Chuang, Science **336**, 563 (2012).
[11] J.-Ph. Reid, A. Juneau-Fecteau, R. T. Gordon, S. René de Cotret, N. Doiron-Leyraud, X. G. Luo, H. Shakeripour, J. Chang, M. A. Tanatar, H. Kim, R. Prozorov, T. Saito, H. Fukazawa, Y. Kohori, K. Kihou, C. H. Lee, A. Iyo, H. Eisaki, B. Shen, H.-H. Wen, and L. Taillefer, Supercond. Sci. Technol. **25**, 084013 (2012).
[12] S. V. Borisenko, V. B. Zabolotnyy, A. A. Kordyuk, D. V. Evtushinsky, T. K. Kim, I. V. Morozov, R. Follath, and B. Büchner, Symmetry **4**, 251 (2012).
[13] A. D. Christianson, E. A. Goremychkin, R. Osborn, S. Rosenkranz, M. D. Lumsden, C. D. Malliakas, I. S. Todorov, H. Claus, D. Y. Chung, M. G. Kanatzidis, R. I. Bewley, and T. Guidi, Nature (London) **456**, 930 (2008).
[14] J.-P. Castellan, S. Rosenkranz, E. A. Goremychkin, D. Y. Chung, I. S. Todorov, M. G. Kanatzidis, I. Eremin, J. Knolle, A. V. Chubukov, S. Maiti, M. R. Norman, F. Weber, H. Claus, T. Guidi, R. I. Bewley, and R. Osborn, Phys. Rev. Lett. **107**, 177003 (2011).
[15] D. S. Inosov, J. T. Park, P. Bourges, D. L. Sun, Y. Sidis, A. Schneidewind, K. Hradil, D. Haug, C. T. Lin, B. Keimer, and V. Hinkov, Nature Phys. **6**, 178 (2009).
[16] C. T. Chen, C. C. Tsuei, M. B. Ketchen, Z. A. Ren, and Z. X. Zhao, Nature Phys. **6**, 260 (2010).
[17] T. Hanaguri, S. Niitaka, K. Kuroki, and H. Takagi, Science **328**, 474 (2010).
[18] T. Hänke, S. Sykora, R. Schlegel, D. Baumann, L. Harnagea, S. Wurmehl, M. Daghofer, B. Büchner, J. van den Brink, and C. Hess, Phys. Rev. Lett. **108**, 127001 (2012).
[19] S. Chi, S. Grothe, R. Liang, P. Dosanjh, W. N. Hardy, S. A. Burke, D. A. Bonn, and Y. Pennec, Phys. Rev. Lett. **109**, 087002 (2012).
[20] S. Grothe, Shun Chi, P. Dosanjh, R. Liang, W. N. Hardy, S. A. Burke, D. A. Bonn, and Y. Pennec, Phys. Rev. B **86**, 174503 (2012).
[21] X. C. Wang, Q. Q. Liu, Y. X. Lv, W. B. Gao, L. X. Yang, R. C. Yu, F. Y. Li, and C. Q. Jin, Solid State Commun. **148**, 538 (2008).
[22] J. H. Tapp, Z. Tang, B. Lv, K. Sasmal, B. Lorenz, P. C. W. Chu, and A. M. Guloy, Phys. Rev. B **78**, 060505(R) (2008).
[23] M. J. Pitch, D. R. Park, P. Adamson, S. J. C. Herkelrath, A. T. Boothroyd, R. M. Ibberson, M. Brunelli, and S. J. Clarke, Chem. Commun. **45**, 5918 (2008).
[24] A. Lankau, K. Koepernik, S. Borisenko, V. Zabolotnyy, B. Büchner, J. van den Brink, and H. Eschrig, Phys. Rev. B **82**, 184518 (2010).
[25] S. V. Borisenko, V. B. Zabolotnyy, D. V. Evtushinsky, T. K. Kim, I. V. Morozov, A. N. Yaresko, A. A. Kordyuk, G. Behr, A. Vasiliev, R. Follath, and B. Büchner, Phys. Rev. Lett. **105**, 067002 (2010).
[26] A. A. Kordyuk, V. B. Zabolotnyy, D. V. Evtushinsky, T. K. Kim, I. V. Morozov, M. L. Kulić, R. Follath, G. Behr, B. Büchner, and S. V. Borisenko, Phys. Rev. B **83**, 134513 (2011).
[27] T. Hanaguri, K. Kitagawa, K. Matsubayashi, Y. Mazaki, Y. Uwatoko, and H. Takagi, Phys. Rev. B **85**, 214505 (2012).
[28] C. Hess, S. Sykora, T. Hänke, R. Schlegel, D. Baumann, V. B. Zabolotnyy, L. Harnagea, S. Wurmehl, J. van den Brink, and B. Büchner, Phys. Rev. Lett. **110**, 017006 (2013).
[29] B. Zeng, D. Watanabe, Q. R. Zhang, G. Li, T. Besara, T. Siegrist, L. Y. Xing, X. C. Wang, C. Q. Jin, P. Goswami, M. D. Johannes, and L. Balicas, Phys. Rev. B **88**, 144518 (2013).
[30] H. Kontani and S. Onari, Phys. Rev. Lett. **104**, 157001 (2010).
[31] P. M. R. Brydon, M. Daghofer, C. Timm, and J. van den Brink, Phys. Rev. B **83**, 060501 (2011).
[32] P. Jeglič, A. Potočnik, M. Klanjšek, M. Bobnar, M. Jagodič, K. Koch, H. Rosner, S. Margadonna, B. Lv, A. M. Guloy, and D. Arčon, Phys. Rev. B **81**, 140511 (2010).
[33] Z. Li, Y. Ooe, X.-C. Wang, Q.-Q. Liu, C.-Q. Jin, M. Ichioka, and G.-Q. Zheng, J. Phys. Soc. Jpn **79**, 083702 (2010).
[34] L. Ma, J. Zhang, G. F. Chen, Weiqiang Yu, Phys. Rev. B **82**, 180501 (2010).
[35] S. H. Baek, L. Harnagea, S. Wurmehl, B. Büchner, and H. J. Grafe, J. Phys.: Condens. Matter **25**, 162204 (2013).
[36] J. D. Wright, M. J. Pitcher, W. Trevelyan-Thomas, T. Lancaster, P. J. Baker, F. L. Pratt, S. J. Clarke, and S. J. Blundell, Phys. Rev. B **88**, 060401 (2013).
[37] C. Platt, R. Thomale, and W. Hanke, Phys. Rev. B **84**, 235121 (2011).
[38] Y. Wang, A. Kreisel, V. B. Zabolotnyy, S. V. Borisenko, B. Büchner, T. A. Maier, P. J. Hirschfeld, and D. J. Scalapino, Phys. Rev. B **88**, 174516 (2013).
[39] M. Wang, M. Wang, H. Miao, S. V. Carr, D. L. Abernathy, M. B. Stone, X. C. Wang, L. Xing, C. Q. Jin, X. Zhang, J. Hu, T. Xiang, H. Ding, and P. Dai, Phys. Rev. B **86**, 144511 (2012).
[40] M. Eschrig, Adv. Phys. **55**, 47 (2006).
[41] S. Johnston and T. P. Devereaux, Phys. Rev. B **81**, 214512 (2010).
[42] I. Morozov, A. Boltalin, O. Volkova, A. Vasiliev, O. Kataeva, U. Stockert, M. Abdel-Hafiez, D. Bombor, A. Bachmann, L. Harnagea, M. Fuchs, H.-J. Grafe, G. Behr, R. Klingeler, S. Borisenko, C. Hess, S. Wurmehl, and B. Büchner, Cryst. Growth Des. **10**, 4428 (2010).
[43] H. Eschrig and K. Koepernik, Phys. Rev. B **80**, 104503 (2009).
[44] J. Ferber, K. Foyevtsova, R. Valenti, and H. O. Jeschke, Phys. Rev. B **85**, 094505 (2012).
[45] Y.-Y. Zhang, C. Fang, X. Zhou, K. Seo, W.-F. Tsai, B. A. Bernevig, and J. Hu, Phys. Rev. B **80**, 094528 (2009).
[46] M. Tinkham, *Introduction to Superconductivity* (McGraw-Hill, New York,1996).
[47] T. Das and A. V. Balatsky, J. Phys: Condens. Mat. **24**, 182201 (2012).
[48] S. Sykora and P. Coleman, Phys. Rev. B **84**, 054501 (2011).
[49] T. Hajiri, T. Ito, R. Niwa, M. Matsunami, B. H. Min, Y. S. Kwon, and S. Kimura, Phys. Rev. B **85**, 094509 (2012).
[50] By changing $\mathbf{k}_{||}$ one also changes the corresponding k_z, such that the measured momenta belong to a curved surface in $\mathbf{k}$ space. However, with 21.2 eV photons and $V_0 = 15.4$ eV, k_z varies from $5.9\pi/c$ to $5.3\pi/c$ over the Γ to M range in $k_{||}$, which allows us to approximate the measured surface simply as a $k_{||}$ plane.
[51] I. I. Mazin, D. J. Singh, arXiv:1007.0047.
[52] T. Hanaguri, Y. Kohsaka, J. C. Davis, C. Lupien, I. Yamada, M. Azuma, M. Takano, K. Ohishi, M. Ono, and H. Takagi, Nature Phys. **3**, 865 (2007).
[53] K. Fujita, I. Grigorenko, J. Lee, W. Wang, J. X. Zhu, J. C. Davis, H. Eisaki, S. Uchida, and A. V. Balatsky, Phys. Rev. B **78**, 054510 (2008).
[54] T. Hanaguri, Y. Kohsaka, M. Ono, M. Maltseva, P. Coleman, I. Yamada, M. Azuma, M. Takano, K. Ohishi, and H. Takagi, Science **323**, 923 (2009).